

Self-Supervised Training with Autoencoders for Visual Anomaly Detection

Alexander Bauer

Abstract—Deep convolutional autoencoders provide an effective tool for learning non-linear dimensionality reduction in an unsupervised way. Recently, they have been used for the task of anomaly detection in the visual domain. By optimising for the reconstruction error using anomaly-free examples, the common belief is that a corresponding network should fail to accurately reconstruct anomalous regions in the application phase. This goal is typically addressed by controlling the capacity of the network by either reducing the size of the bottleneck layer or enforcing sparsity constraints on its activations. However, neither of these techniques does explicitly penalise reconstruction of anomalous signals often resulting in poor detection. We tackle this problem by adapting a self-supervised learning regime, which allows to use discriminative information during training focusing on the data manifold by means of a modified reconstruction error. This regularizes the model to produce locally consistent reconstructions, while replacing irregularities by acting as a filter for anomalous patterns. In contrast to related approaches, inference with our method is very efficient during training and prediction processing the entire input image in one single step. Our experiments on the MVTEC AD dataset demonstrate high recognition and localisation performance of the proposed method. On the texture-subset, in particular, our approach consistently outperforms a bunch of recent anomaly detection methods by a big margin.

Index Terms—Anomaly detection, autoencoders, neural inpainting.



1 INTRODUCTION

THE task of anomaly detection in a broad sense corresponds to searching for patterns which considerably deviate from some concept of normality. Visual anomaly detection specifically aims to detect and locate anomalous regions in imagery data. The criteria of what is normal and what is an anomaly can be very subtle and highly application dependent. The existing detection algorithms [1], [2], [3], [4], [5], [6], [7], [8], [9], [10], [11] typically assume the availability of normal examples only, while the anomalous examples are very scarce and are usually used to tune the hyperparameters of a corresponding model. The prevalent direction of research in the last two decades was focusing on the so-called one-class classifiers [1], [12] which aim at learning a tight decision boundary around the normal examples in a feature space and define a distance-based anomaly score relative to the center of the training data. The success of this approach strongly depends on the availability of suitable features. Therefore, it usually allows for detection of outliers only, which greatly deviate from the normal structure. In practice, however, we are often interested in more subtle deviations, which require a good representation of the data manifold. The same applies to the combined approach based on training deep neural networks (DNNs) directly with the one-class objective [2], [13], [14]. Although this objective encourages the network to concentrate the training data in a small region in the feature space, there is no explicit motivation for anomalous examples unseen during training to be mapped outside of the decision boundary. In other words, the one-class objective gives preference to models which map its input domain to a narrower region and does

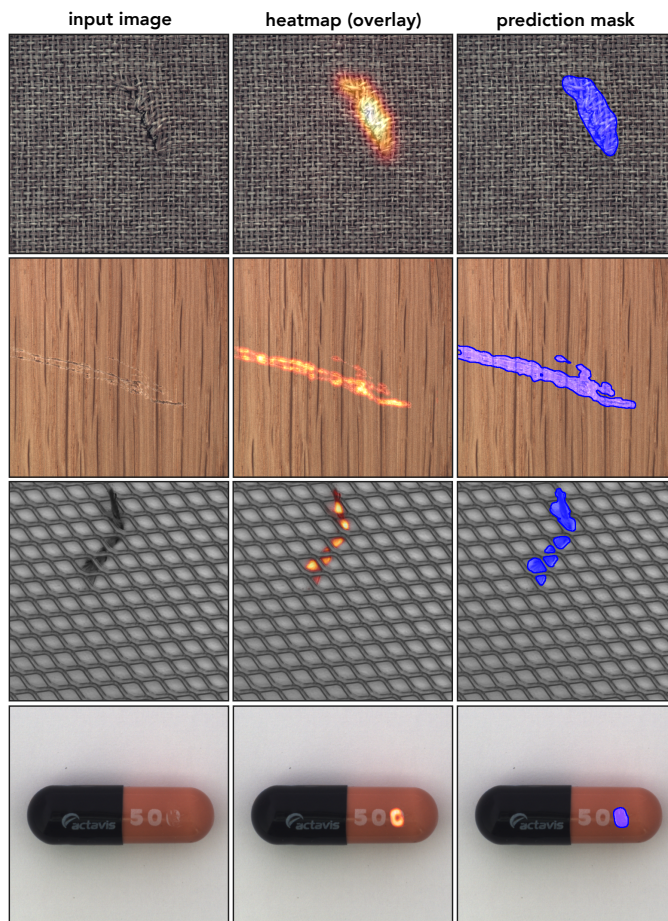


Fig. 1. Some anomaly detection results of our approach. Each row shows the input image, the overlay of a corresponding anomaly heatmap, and the resulting prediction mask, respectively.

not explicitly focus on separating anomalous examples from the normal data.

Recently, deep autoencoders have been used for the task of anomaly detection in the visual domain [3], [15], [16]. Unlike one-class based approaches, they additionally allow for locating the anomalous regions in images by leveraging the pixel-wise nature of a corresponding training objective. By optimizing for the reconstruction error using anomaly-free examples, the common belief is that a corresponding network should fail to accurately reconstruct anomalous regions in the application phase. This goal is typically addressed by controlling the capacity of the network by either reducing the size of the bottleneck layer or enforcing some sparsity constraints on the inner activations [17], [18]. However, neither of these techniques does explicitly penalize reconstruction of anomalous signals often resulting in a poor detection. This is similar to the issue related to training with the one-class objective, where no explicit mechanism exists for preventing anomalous data points from being mapped to the normal region. In fact, an autoencoder optimized for the reconstruction error mainly aims to compress and accurately reconstruct the input images and doesn't care much about the actual distinction between normal and anomalous pixels. As a result, the reconstruction errors for the anomalous and normal regions can be very similar preventing reliable detection and localization.

In this paper, we propose a self-supervised learning framework, which introduces discriminative information during training to prevent good reconstruction of anomalous patterns in the testing phase. We begin with an observation that the abnormality of a region in an image can be partially characterized according to how well it can be reconstructed from the context of the surrounding pixels. Imagine an image where a small patch has been cut out by setting the corresponding pixel values to zeros. We can try to reconstruct this patch by extrapolating the surrounding pixel values according to our knowledge about the patch distribution of the training data. If the reconstruction significantly deviates from the original image, we consider a corresponding patch to be anomalous and normal otherwise. Following this intuition, we feed partially distorted images to the network during training while forcing it to reconstruct the original content similar to the task of neural image completion [19], [20], [21], [22], [23]. However, instead of setting the individual pixel values to zeros – as for the completion task, we apply a patch transformation, which approximately preserves the color distribution of the distorted regions, making it more difficult for the network to realize which image regions have been modified. In order to succeed, the network now must learn features which are suitable for accomplishing two different tasks: a) detection of image regions deviating from an expected pattern and b) reconstruction of such regions from the neighboring pixel sets. Since this approach utilizes no explicit information (e.g., label mask) about the location of the anomalous regions – unlike for the task of semantic segmentation, for example – it regularizes the model to produce locally consistent reconstructions while replacing irregularities, therefore, acting as a filter for anomalous patterns.

Formally, the mapping implemented by a corresponding DNN approximates a non-linear orthogonal projection of

partially corrupted images onto the data manifold consisting of anomaly-free examples. Given an orthogonal projection, we can naturally define the notion of anomalous examples according to their distance from the data manifold. Furthermore, we can identify the actual anomalous regions within the images by means of the pixel-wise reconstruction error. We also note that the prediction process is very efficient as the entire image is processed in a single step - in contrast to related reconstruction ideas based on the sliding window approach [3], [16]. Figure 1 illustrates a few examples to give a sense of visual quality of the resulting segmentation masks when training according to our approach.

There is one potential issue with the above approach due to anomaly score being defined by the reconstruction error, which is sensitive to the variation of pixel intensities in the following sense. On the one hand, a high variation in pixel intensities (e. g. pepper noise) in the normal regions is likely to result in false positive detections. On the other hand, anomalous regions with a strong structural deviation might not be detected, if the color distribution of the corresponding pixels is of low contrast resulting in a small reconstruction error. To address this issue, we further experiment with our approach by modifying the training objective such that the network is penalized for producing a high reconstruction error in the normal regions while being rewarded for a higher reconstruction error in the distorted areas. The resulting network shows a kind of hybrid behavior. On the one hand it aims at reconstructing the normal regions and on the other hand it amplifies the reconstruction error for the anomalous regions by further disturbing the corresponding area acting almost as a segmentation network. As we demonstrate in the experimental section, this modification might potentially improve the localization accuracy of the anomalous regions in comparison to our original idea.

The rest of the paper is organized as follows. In Section 2 we first discuss the main differences of our approach to the related works. In Section 3 we formally introduce the proposed framework including training procedure, data generation process, and model architecture. In Section 4 we evaluate the performance of our approach and provide the experimental results for the task of visual anomaly detection based on the publicly available MVTEC AD dataset [24], [25]. We finish our discussion with a conclusion in Section 5.

2 RELATED WORKS

In the context of automatic surface inspection, [3] proposed an anomaly detection approach based on neural image completion. Specifically, they train a convolutional neural network (CNN) to reconstruct small image patches for which a rectangular center area has been cut out. Using sliding window approach during prediction phase they compute a reconstruction error on the whole input image. To be able to complete the central region, a model must learn meaningful features, which allow to interpolate the local context. Although presenting an inspiring idea, this approach has two significant issues. First, cutting out an area prevents reconstruction of locally confined patterns, which cannot be computed from the context. Regardless if

a corresponding pattern is anomalous or normal, it will be lost during the completion process resulting in a high reconstruction error. Second, the presented idea relies on a sliding window approach to detect anomalies at different image locations resulting in a slower inference during prediction phase. In contrast, we process the entire input image in one single step. Furthermore, our training objective does not rely on reconstruction of missing patches but rather aims at reproducing normal regions within the input image and either filtering anomalous patterns or enlarging the reconstruction difference for the areas which are inconsistent with their surrounding context. In particular, no information about the image is lost during the prediction phase allowing for an accurate reconstruction of the anomaly-free areas, which in turn improves the resulting detection performance of the anomalous regions.

Another previous work [5] aims at preventing reconstruction of anomalous patterns by projecting the input images to the normal regions in the latent space. The training and prediction phase are performed in two steps. Specifically, the authors first adopt a variational autoencoder as the reconstruction model to get a discrete latent space of normal samples. Then a deep autoregressive model is used to estimate the probability distribution of the training data in the latent space. In the detection stage this autoregressive model is used to determine which parts of the signal deviate from the data distribution in the latent space and should be resampled to yield a restored image, which is closest to the anomaly input. In contrast, our approach requires a single inference pass in both phases and requires no additional resampling.

More recent works [16], [26] also rely on the idea of image inpainting originally introduced in [3]. The work in [26] replaces the sliding window procedure by a different approach. First the input image is divided in a grid of cells and a number of images is created by randomly removing some cells in the original image. Inference is then performed on each single image and the resulting reconstruction is assembled from partial reconstructions of all images. The method in [16] further rely on the sliding window idea, but unlike other methods use a self-attention based transformer instead of convolutional autoencoders. According to the authors, one drawback of their approach is the increased training time due to transformer architecture. Both methods achieve very accurate results on the MVTEC AD dataset [24], [25] as we demonstrate in the experimental section.

Another accurate method proposed in [15], is similar to our idea in the sense that it also modifies input images to artificially create anomalous regions using a specific Cut&Paste augmentation technique. Unlike our method, however, it is a two-stage approach relying on training an additional binary classifier for detection and localization of the anomalous regions based on the visual explanation algorithm called GradCAM [27].

3 METHODOLOGY

We now introduce a self-supervised framework for training deep convolutional autoencoders to detect anomalous regions in images. More precisely, we describe the objective function, the data generation process during training, and

our choice of the model architecture. As a closing remark, we provide a geometric interpretation of the resulting model as an approximation of a non-linear orthogonal projection of anomalous examples onto the data manifold populated by the anomaly-free images.

3.1 Training Objective

We use $F: [0, 1]^{n \times m \times 3} \rightarrow [0, 1]^{n \times m \times 3}$, $n, m \in \mathbb{N}$ to denote a mapping related to a DNN that implements an autoencoder with input and output tensors corresponding to color images. Furthermore, we denote by $X \in [0, 1]^{n \times m \times 3}$ an original image and by \hat{X} a copy of X , which has been partially modified. The modified regions within \hat{X} are marked by a binary ¹ mask $M \in \{0, 1\}^{n \times m \times 3}$, where \bar{M} denotes a corresponding complement. Given this notation, our training objective can be written as follows:

$$\mathcal{L}(\hat{X}, X) = \frac{\lambda}{\|\bar{M}\|_1} \cdot \|\bar{M} \odot (F(\hat{X}) - X)\|_2 + \frac{(1 - \lambda)}{\|M\|_1} \cdot \|M \odot (F(\hat{X}) - X)\|_2 \quad (1)$$

where \odot denotes an element-wise tensor multiplication and $\lambda \in [0, 1]$ is a weighting parameter for controlling the importance of the two terms during training. $\|\cdot\|_p$ for $p \in \mathbb{N}_+$ denotes the L^p -norm on a corresponding tensor space. In terms of supervised learning, we feed a partially modified image \hat{X} as input to the network, which we train to reconstruct the original image X representing the ground truth label.

By minimizing the above objective, a corresponding autoencoder aims at learning to perform two tasks. The first term pushes the network towards an accurate reconstruction of the masked input image $\bar{M} \odot X$ from a latent space, while the second term requires the network to correct corrupted regions $M \odot \hat{X}$ by restoring the original content. Altogether, the objective in equation (1) steers the behavior of a corresponding autoencoder to produce locally consistent reconstructions of the input images while replacing irregularities, acting, in some sense, as a filter for anomalous patterns. The second column in Figure 2 shows some reconstruction examples produced by two different models trained either on wooden or carpet surface images from the MVTEC AD dataset without defects [24]. We can see how normal regions are accurately replicated by each model, while irregularities (e.g., scratches or tears) are replaced by locally consistent patterns.

Given a trained autoencoder F and an input image \hat{X} , we can perform anomaly detection by thresholding a corresponding anomaly heatmap computed by averaging the term $(F(\hat{X}) - \hat{X})^2$ over the color channels. To get a more robust result we smooth the anomaly heatmap using a gaussian filter before thresholding. The complete detection procedure is summarized in Figure 2.

In some cases, a model trained using objective (1) can fail to produce accurate detection results. As already mentioned

1. For the sake of simplicity we first restrict the mask M and its complement \bar{M} to be binary. Later we will relax this assumption and consider real-valued tensors $M \in [0, 1]^{n \times m \times 3}$. A corresponding complement is then defined as $\bar{M} = \mathbb{1} - M$ where $\mathbb{1}$ represents a tensor of the same size as M having value 1 at each index.

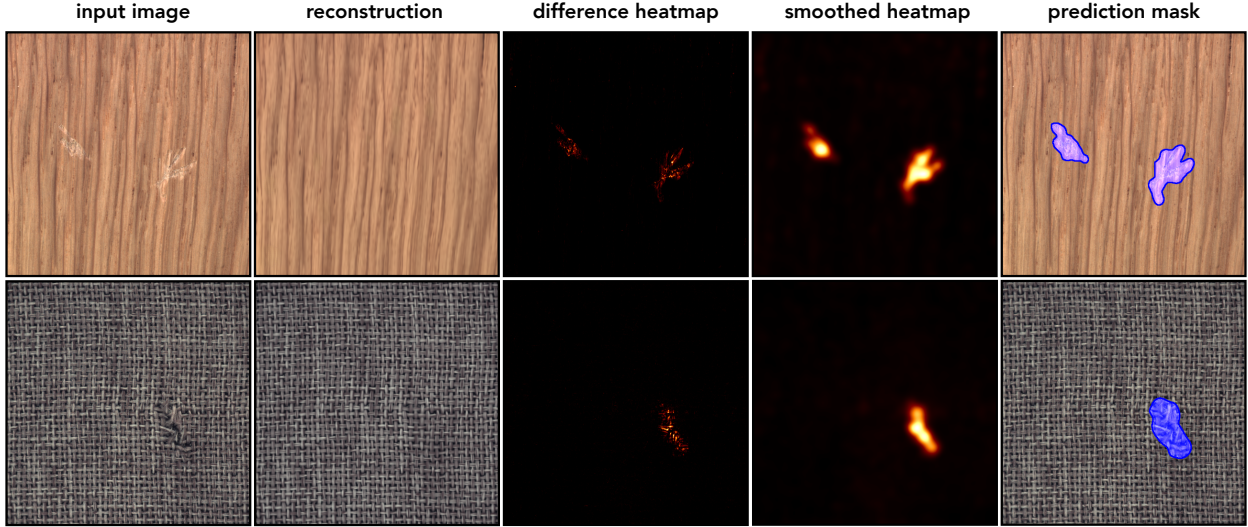


Fig. 2. Illustration of how anomaly detection is performed by thresholding a computed anomaly heatmap on two different examples: wooden surface (first row) and carpet (second row). In each row the first column represents the input image \hat{X} to our model identified with the mapping F . The second column shows the output of the model $F(\hat{X})$ being a reconstruction of the input image. The third column shows the difference heatmap computed according to $(F(\hat{X}) - \hat{X})^2$. The fourth column shows the result of smoothing the difference heatmap by applying a gaussian filter and represents our final anomaly heatmap to be used for detection. The last column visualizes the binary prediction mask (in blue color) computed by thresholding the anomaly heatmap from the previous column.

in the introduction, a problem with the above approach is that the reconstruction error is sensitive to the pixel intensities. Anomalous regions even with a strong structural deviation from normal patterns but of low contrast might not be detected, if the reconstruction $F(\hat{X})$ has similar pixel intensities as the input \hat{X} (see Figure 6 for an example). One way to address this problem is to use a GMS-based smoothing scheme proposed in [16], [26] to generate more robust anomaly heatmap. Unfortunately, this can also amplify the background noise in the image increasing the number of false positive detections. Here, we investigate a different idea by adjusting our training objective in (1) to reward a higher reconstruction error in the distorted areas as follows:

$$\mathcal{L}(\hat{X}, X) = \frac{\lambda}{\|\bar{M}\|_1} \cdot \left\| \bar{M} \odot (F(\hat{X}) - X) \right\|_2 - \frac{(1-\lambda)}{\|\hat{X} - X\|_1} \cdot \left\| |\hat{X} - X| \odot (F(\hat{X}) - X) \right\|_2 \quad (2)$$

Note the minus sign between the two terms in the above objective. The first term encourages the network to produce an accurate reconstruction of the normal regions, while the second term amplifies the reconstruction error for the modified area increasing the contrast in the resulting anomaly heatmap. Figure 3 illustrates some reconstruction results of a corresponding model when trained using the objective (2). Note how the anomalous regions are emphasized in the reconstruction image resembling, in some sense, the performance of a model trained for the task of semantic segmentation. In order to decrease the loss value, the network has to put more attention on the task of locating the anomalous regions potentially improving the final localization performance. For anomalous regions of low contrast this improvement can be dramatic as we show in the experimental section. Figure 6 provides some

examples illustrating the qualitative difference between the two objectives in such a case.

There is one further detail in the objective (2) required to prevent the following unwanted effect. Depending on the type of transformation producing \hat{X} from X , the objective (2) can put too much weight on the second term. Namely, the loss can be easily decreased by setting the pixel values $F(\hat{X})$ within the mask M to achieve maximal difference to the corresponding pixels in X completely ignoring the actual pixel difference $|\hat{X} - X|$. In particular, if some regions have exactly the same pixel values in both images, the objective (2) still encourages the network to increase the reconstruction error for these regions. We tackle this

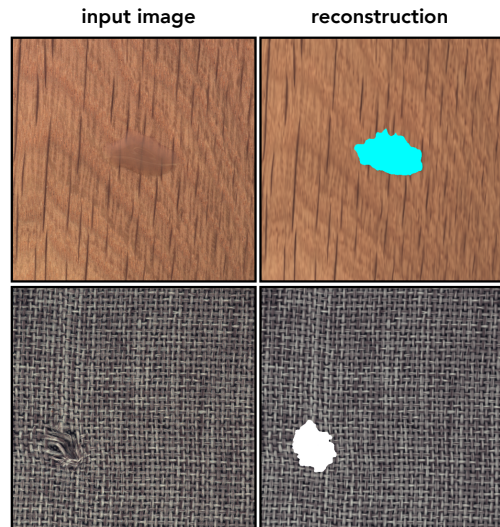


Fig. 3. Illustration of the reconstruction effect of two models trained either on the wooden or carpet surface images (without defects) from the MVTec AD dataset using objective (2).

by replacing the binary mask M with a real-valued mask $|\hat{X} - X| \in [0, 1]^{n \times m \times 3}$, therefore, reducing the importance of the second term according to the relative pixel difference. We note that our image modification procedure ensures that inequality $\|\hat{X} - X\|_1 > 0$ always holds.

3.2 Data Generation and Training

Since we use a self-supervised approach we need to provide a training data consisting of input-output pairs. The ground truth outputs are given by the original images corresponding to the normal examples. The inputs are generated from these images by partially modifying some regions as follows. For each image X , in the first step we randomly sample the size and the location of a patch to be modified. Then a corresponding patch is extracted and passed through an elastic deformation process. Additionally, we randomly define a shape mask to smoothly glue the content of the modified patch with the original patch. In the last step the shape mask is embedded in a two-dimensional zero-array at the location chosen in the first step to create a global mask represented by a real-valued tensor $M \in [0, 1]^{n \times m \times 3}$. Finally, a corresponding content of the original image X is replaced by the modified patch giving a corrupted image \hat{X} . The whole procedure is illustrated in Figure 4.

During training we sample images from the ground truth data representing the outputs from which we generate distorted inputs to be passed to the network. We experimented with different transformations of the original images like simple cut-out, patch swapping and elastic deformation with the latter providing the best results. We also found that it can be useful (depending on the data) to vary the brightness of modified patches. Furthermore, we use a progressive training scheme gradually increasing the size of the input images while keeping the same resolution over the course of the training phase. During testing phase there is no input modification and images are passed unchanged to the network. Anomalous regions are then detected by thresholding a corresponding heatmap computed from the difference between the inputs and the outputs produced by the autoencoder.

3.3 Model

We follow an established architecture of deep autoencoders, where the encoder is build from layers gradually decreasing spatial dimension and increasing the number of feature maps while the decoder reverses this process by increasing the spatial dimension and decreasing the number of channels. An important detail here is that additionally to the standard convolutions we exploit the dilated convolutions for approximating higher order dependencies between the individual pixels and their local neighbourhood. An overview of the whole architecture is given in Table 1. Here, after each convolution *Conv.* (except in the last layer) we use batch normalisation and rectified linear units (ReLU) as the activation function. Max-pooling *MaxPool.* is applied to reduce the spatial dimension of the intermediate feature maps. *Transp. Conv.* denotes the convolution transpose operation and also uses batch normalisation with ReLUs. In the last layer we use a sigmoid activation function without batch normalisation. We observed that using batch

normalisation in the last layer sometimes can lead to strong gridding effects in the reconstruction. $\text{SDC}_{1,2,4,8,16,32}$ refers to a stacked dilated convolution where multiple dilated convolutions are stacked together. The corresponding subscript $\{1, 2, 4, 8, 16, 32\}$ denotes the dilation rates of the six individual convolutions in each stack. After each stack we add an additional convolutional layer with the kernel size 3×3 and the same number of feature maps as in the stack followed by a batch normalisation and ReLU activation.

TABLE 1
Model architecture.

Layer Type	Number of Filters	Filter Size	Output Size
Conv.	64	3×3	$512 \times 512 \times 32$
Conv.	64	3×3	$512 \times 512 \times 32$
MaxPool.		$2 \times 2 / 2$	$256 \times 256 \times 32$
Conv.	128	3×3	$256 \times 256 \times 64$
Conv.	128	3×3	$256 \times 256 \times 64$
MaxPool.		$2 \times 2 / 2$	$128 \times 128 \times 64$
Conv.	256	3×3	$128 \times 128 \times 128$
Conv.	256	3×3	$128 \times 128 \times 128$
MaxPool.		$2 \times 2 / 2$	$64 \times 64 \times 128$
$\text{SDC}_{1,2,4,8,16,32}$	64×6	5×5	$64 \times 64 \times 384$
$\text{SDC}_{1,2,4,8,16,32}$	64×6	5×5	$64 \times 64 \times 384$
$\text{SDC}_{1,2,4,8,16,32}$	64×6	5×5	$64 \times 64 \times 384$
$\text{SDC}_{1,2,4,8,16,32}$	64×6	5×5	$64 \times 64 \times 384$
Transp. Conv.	256	$3 \times 3 / 2$	$128 \times 128 \times 256$
Conv.	256	3×3	$128 \times 128 \times 256$
Conv.	256	3×3	$128 \times 128 \times 128$
Transp. Conv.	128	$3 \times 3 / 2$	$256 \times 256 \times 128$
Conv.	128	3×3	$256 \times 256 \times 128$
Conv.	128	3×3	$256 \times 256 \times 64$
Transp. Conv.	64	$3 \times 3 / 2$	$512 \times 512 \times 64$
Conv.	64	3×3	$512 \times 512 \times 64$
Conv.	64	3×3	$512 \times 512 \times 32$
Conv.	3	1×1	$512 \times 512 \times 3$

3.4 Geometric Interpretation

In the following, we would like to give a geometric perspective on the mapping F resulting from training a reconstruction model according to the objective (1). For this purpose, we first introduce an auxiliary notation. For each formal statements we provide a proof in the supplements.

We identify each image tensor $X \in \mathbb{R}^{n \times m \times 3}$ with a column vector $\mathbf{x} \in \mathbb{R}^N$, $N := n \cdot m \cdot 3$ and denote by $S \subset \{1, \dots, N\}$ and $\bar{S} := \{1, \dots, N\} \setminus S$ a set of pixel indices and its complement, respectively. We write $\mathbf{x}_S \in \mathbb{R}^{|S|}$ to denote a corresponding restriction of $\mathbf{x} \in \mathbb{R}^N$ to the indices in S . Regarding the task of anomaly detection, we denote by D a data manifold containing only normal images. For example, D could be a set of images of wooden surface without defects. Given D , we define a superset ² $\hat{D} := \{\hat{\mathbf{x}} \in \mathbb{R}^N \mid \exists \mathbf{x} \in D, S \subseteq \{1, \dots, N\}: \hat{\mathbf{x}}_S = \mathbf{x}_S\} \supseteq D$. That is, each (corrupted) image $\hat{\mathbf{x}} \in \hat{D} \setminus D$ can be seen as being generated from a normal image $\mathbf{x} \in D$ by partial

2. Note that we can always choose $|S| = N$. In that case $\hat{D} = \mathbb{R}^N$. To keep the notation simple we omit additional requirement on $|S|$ in the definition of \hat{D} and assume implicitly that S is constrained according to some constant $|S| \leq k$ which we treat as a hyperparameter depending on the maximal size of the anomalous regions.

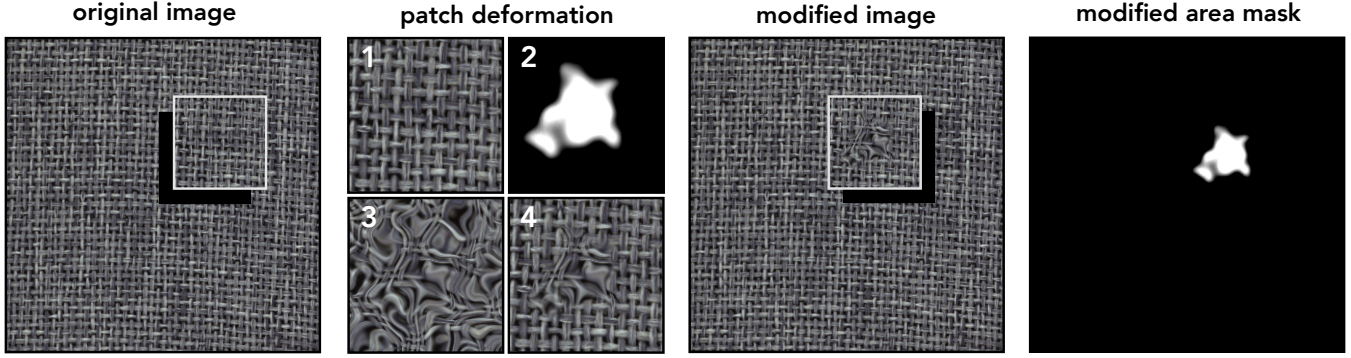


Fig. 4. Illustration of the process for generating artificial distortions within the training images. In the first step (see first image) we randomly choose the size and location of a patch to be modified. In the second step (see second image) a corresponding patch is extracted and transformed using elastic deformation by introducing gaussian distortions. Also a real-valued shape mask is created for the content of the transformed patch. The final modified patch to be placed in the original image is created according to the formula $X_4 = X_2 \odot X_3 + (\mathbb{1} - X_2) \odot X_1$ where X_1, X_2, X_3, X_4 represent the four patches in the second image. In the last step the shape mask is embedded in a 2-dimensional zero-array to create a global mask $M \in [0, 1]^{n \times m \times 3}$ and a corresponding content of the original image X is replaced by masking the modified patch (see the result X_4) giving the modified image \hat{X} .

modification according to a set of pixel indices in S . According to the training objective (1), the corresponding model aims at learning a mapping F which maps each $\hat{x} \in \hat{D}$ to some $F(\hat{x}) = x \in D$ where $\hat{x}_{\bar{S}} = x_{\bar{S}}$ and $S \subset \{1, \dots, N\}$ with $0 < |S| < N$.

Based on the introduced notation, we now can state the following fact. Namely, the restriction $F|_{\hat{D}}$ resembles an orthogonal projection³ of locally corrupted examples $\hat{x} \in \hat{D}$ onto the data manifold D populated by the normal images (without defects). We emphasise this fact in the proposition below where $B_\epsilon(x_S) := \{z_S \in \mathbb{R}^{|S|} : \|x_S - z_S\| \leq \epsilon\}$ denotes a closed ball of radius ϵ around x_S .

Proposition 1. Let $x, y \in \mathbb{R}^N$ and $S \subset \{1, \dots, N\}$. For all $\hat{x} \in \mathbb{R}^N$ with $\hat{x}_S \in B_\epsilon(x_S)$, $\epsilon := \|x_S - y_S\|$ and $\hat{x}_{\bar{S}} = x_{\bar{S}}$, the following implication is true:

$$\|x_S - y_S\| \leq \|x_{\bar{S}} - y_{\bar{S}}\| \implies \|\hat{x} - x\| \leq \|\hat{x} - y\|. \quad (3)$$

In particular, the above proposition holds for all \hat{x}_S which can be represented as a convex combination of x_S and y_S including the important boundary case: $\hat{x}_S = y_S$. By setting $\epsilon = \inf_{z_S \in D|_S} \|x_S - z_S\|$ for a given x , we can ensure that the implication in (3) holds simultaneously for all y .

Next, we turn our attention to the premise in (3). One simple way to increase the likelihood of this premise to be true is to restrict ourselves to images where all pixels are identically distributed, that is, $P(x_i) = P(x_j)$ for all $i, j \in \{1, \dots, N\}$. Note that this restriction allows for complex patterns and includes all examples corresponding to the texture categories in the MVTEC AD data set. We support this claim by empirical evaluation in Figure 5 in Section 4. Based on the previous assumption, we can state the following proposition.

Proposition 2. Let $x, y \in \mathbb{R}^N$ and $P(x)$ be a probability measure with $P(x_i) = P(x_j)$ for all $i, j \in \{1, \dots, N\}$.

Then for all $S \subset \{1, \dots, N\}$ the following equality holds:

$$\mathbb{E} [\|x_S - y_S\|^2 - \|x_{\bar{S}} - y_{\bar{S}}\|^2] = (|S| - |\bar{S}|) \cdot \mu, \quad (4)$$

3. For $\hat{D}, D \subseteq \mathbb{R}^n$ in a metric space (\mathbb{R}^n, d) , we call a (non-linear) mapping $F: \hat{D} \subseteq \mathbb{R}^n \rightarrow D$ an **orthogonal projection** onto D if for each $\hat{x} \in \hat{D}$ the equality $d(\hat{x}, F(\hat{x})) = \inf_{x \in D} d(\hat{x}, x)$ holds.

where $\mu = \mathbb{E} [(x_i - y_i)^2]$ for some $i \in \{1, \dots, N\}$.

It follows directly (due to $\mu > 0$) from equation (4) that $|S| \leq |\bar{S}|$ is a necessary condition in order for our premise $\|x_S - y_S\| \leq \|x_{\bar{S}} - y_{\bar{S}}\|$ to be true. We can further decrease the expected difference in (4) by either decreasing $|S|$ corresponding to the size of the corrupted regions or by increasing the resolution N of the training images.

We note that Proposition 1 is focusing on deformations $\hat{x}_S \in B_\epsilon(x_S)$ which are close to the data manifold D including elastic deformation from the previous Section 3.2 and does not account for some important cases like $\hat{x}_S = \mathbf{0}$. We now briefly discuss this special case making use of the following lemma.

Lemma 1. For all $\hat{x}, x, y \in \mathbb{R}^N$ where $\hat{x}_{\bar{S}} = x_{\bar{S}}$ for some $S \subset \{1, \dots, N\}$ and its complement \bar{S} the inequality

$$\|\hat{x} - x\| \leq \|\hat{x} - y\| \quad (5)$$

holds if and only if

$$\|\hat{x}_S - x_S\|^2 - \|\hat{x}_S - y_S\|^2 \leq \|x_{\bar{S}} - y_{\bar{S}}\|^2. \quad (6)$$

If we can make an assumption that the norm of any two points $x, y \in D$ for an arbitrary S is approximately the same, that is, $\|x_S\| \approx \|y_S\|$, we can expect the inequality $\|x_S\|^2 - \|y_S\|^2 \leq \|x_S - y_S\|^2$ to hold in the most cases. Using the same argument as in Proposition 2 we can increase the likelihood of the inequality $\|x_S - y_S\|^2 \leq \|x_{\bar{S}} - y_{\bar{S}}\|^2$. Then $\|\hat{x} - x\| \leq \|\hat{x} - y\|$ follows directly from Lemma 1.

Given the orthogonality of $F|_{\hat{D}}$, we can naturally measure the degree of abnormality of an image according to the distance $\|\hat{X} - F(\hat{X})\|$ between a corrupted example \hat{X} and its orthogonal projection $F(\hat{X})$ onto the data manifold of defect-free examples.

4 EXPERIMENTAL ANALYSIS

In this section we evaluate the performance of our approach for the task of visual anomaly detection and compare the results with the existing methods.

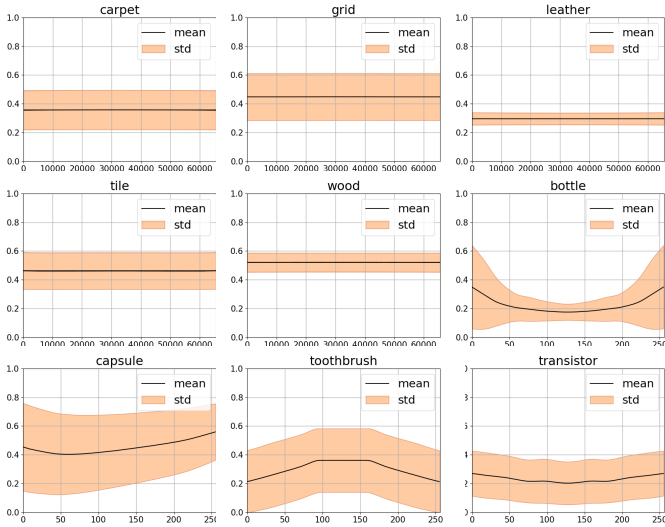


Fig. 5. Illustration of the estimated marginal distribution over pixel values for some categories in the MVTec AD data set. In particular, we can see that all the textures categories satisfy the condition $P(x_i) = P(x_j)$ for all pixels i, j in the image.

4.1 Data and Setup

We used the public MVTec Anomaly Detection dataset [24], [25] in our experiments consisting of 5 texture and 10 object categories. The texture categories cover both regular (carpet, grid) and random pattern cases (leather, tile, wood). This dataset has been widely used as a benchmark for anomaly detection and localization in the manufacturing domain. To increase the amount of the training data we used simple data augmentation like rotation by a multiple of 90 degrees, as well as horizontal and vertical flipping depending on the category.

For each category we trained a separate model according to the architecture in Table 1 by minimizing either the objective (1) or (2). For the texture categories we used the same image resolution of 512×512 pixels. For the object categories we varied the input resolution in the range $\{256, 384, 512\}$. To train the weights of the model we used AdamOptimizer [28] with initial learning rate of 10^{-4} .

To evaluate the localization performance of our model, we report the pixel-wise area under the ROC (AUROC) metric, which is independent of the chosen threshold for the anomaly score. Additionally, we evaluate the AUROC metric on the image-level to estimate the corresponding recognition performance.

4.2 Results

First we provide in Figure 5 empirical evidence justifying our assumption in Proposition 2 concerning the marginal probability distribution over the pixel values for texture categories. More precisely, we estimate the empirical mean and the standard deviation of the pixel values as follows. We resize the images in our training data to 512×512 pixels and compute the corresponding statistics from all sliding windows of the size 256×256 . For the texture categories we show the empirical mean and the standard deviation for each pixel. For the sake of presentation, we visualize the

corresponding statistics for object categories only for pixels which lie on the horizontal line in the middle of the images. In particular, we can see that all the texture categories satisfy the condition $P(x_i) = P(x_j)$ for each pair of pixels i, j .

To evaluate the segmentation accuracy of our model trained with objective (1), we report the pixel-wise AUROC metric in Table 2.

Additionally, we report the AUROC metric on the image-level to estimate the recognition performance and compare our results to the current state-of-the-arts algorithms in Table 3. Our empirical evaluation suggests that training a reconstruction model according to the objective (1), on average, provides more accurate results than the alternative approach with objective (2). We report the corresponding metrics in Table 4 for comparison based on the texture categories in the MVTec AD data set.

Although being less accurate on average, we observed that objective (2) can sometimes provide highly accurate segmentation results. We conjecture that the resulting segmentation accuracy, when training with objective (2), is affected by the choice of the specific transformations, which are used during training to create modified inputs. By adopting the corresponding transformation process according to the expected type of anomalous pattern, a model trained with objective (2) can potentially achieve a higher detection and localization performance. To support this claim, we visualize in Figure 6 the difference in quality of the anomaly heatmaps for the two objectives on a few examples of liquid contamination on the wooden surface. The corresponding columns in the figure show the input image, the ground truth label mask, the anomaly heatmap according to objective (2) using Elastic Deformation for image modification, the anomaly heatmap according to objective

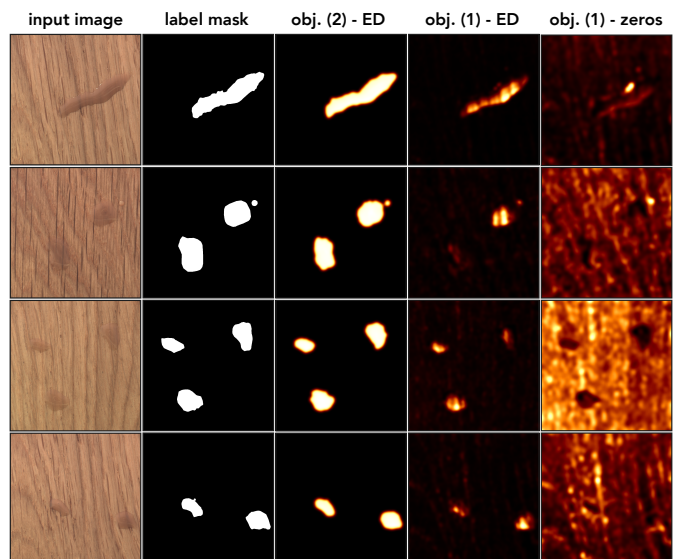


Fig. 6. Illustration of the qualitative performance difference when training either with objective (2) (third column) or (1) (fourth and fifth column) on a few examples of glue drops on the wooden surface. The first two columns show the input images and the ground truth label masks provided with the data set. "ED" indicates that Elastic Deformation has been used for creating modified patches during training. "zeros" indicates that modified area has been cut out by setting the corresponding pixel values to zeros.

TABLE 2

Experimental results for the anomaly segmentation task given as **AUROC** on the pixel-level for each category in the MVTec AD dataset.

Category	AnoGAN [8]	CNNFD [9]	VAE [11]	AE _{SSIM} [4]	FCDD [29]	LSR [5]	RIAD [26]	CutPaste [15]	InTra [16]	Ours
carpet	0.54	0.72	0.78	0.87	0.96	0.94	0.96	0.98	0.99	1.00
grid	0.58	0.59	0.73	0.94	0.91	0.99	0.99	0.98	0.99	1.00
leather	0.64	0.87	0.95	0.78	0.98	0.99	0.99	0.99	0.99	0.99
tile	0.50	0.93	0.80	0.59	0.91	0.88	0.89	0.90	0.94	0.99
wood	0.62	0.91	0.77	0.73	0.88	0.87	0.86	0.95	0.89	0.98
avg. textures	0.58	0.80	0.81	0.78	0.93	0.93	0.94	0.96	0.96	0.99
bottle	0.86	0.78	0.87	0.93	0.97	0.95	0.98	0.98	0.97	0.98
cable	0.86	0.78	0.87	0.82	0.90	0.95	0.94	0.90	0.91	0.96
capsule	0.84	0.84	0.74	0.94	0.93	0.93	0.93	0.97	0.98	0.97
hazelnut	0.87	0.72	0.98	0.97	0.95	0.95	0.96	0.97	0.98	0.98
metal nut	0.76	0.82	0.94	0.89	0.94	0.91	0.92	0.93	0.93	0.97
pill	0.87	0.68	0.83	0.91	0.81	0.95	0.96	0.96	0.98	0.97
screw	0.80	0.87	0.97	0.96	0.86	0.96	0.99	0.97	0.99	0.99
toothbrush	0.90	0.77	0.94	0.92	0.94	0.97	0.99	0.98	0.99	0.99
transistor	0.80	0.66	0.93	0.90	0.88	0.91	0.88	0.93	0.96	0.96
zipper	0.78	0.76	0.78	0.88	0.92	0.98	0.98	0.99	0.99	0.99
avg. objects	0.83	0.77	0.88	0.91	0.91	0.95	0.95	0.96	0.97	0.98
avg. all	0.75	0.78	0.86	0.87	0.92	0.94	0.95	0.96	0.96	0.98

(1) using Elastic Deformation for image modification, and the anomaly heatmap according to objective (1) using the replacement-by-zeros as the image modification technique, respectively.

To summarize, the experimental results show that training our model according to the objective (1) provides (on average) more accurate results for both recognition and localization of the anomalous regions and consistently outperforms the previous methods on the texture categories of the MVTec AD data set. To give a sense of visual quality of the resulting segmentations when training with objective (1), we show a few examples in Figure 1 and further examples in Figure 7.

4.3 Discussion

We presented two different objectives (1) and (2) for training an autoencoder for the task of detecting and segmenting

TABLE 3

Experimental results for the anomaly detection task given as **AUROC** on the image-level for each category in the MVTec AD dataset.

Category	RIAD [26]	CutPaste [15]	InTra [16]	Ours
carpet	0.84	0.93	0.99	0.98
grid	1.00	1.00	1.00	1.00
leather	1.00	1.00	1.00	1.00
tile	0.93	0.93	0.98	1.00
wood	0.93	0.99	0.97	0.99
avg. textures	0.94	0.97	0.99	0.99
bottle	1.00	0.98	1.00	1.00
cable	0.82	0.81	0.70	0.83
capsule	0.88	0.96	0.86	0.84
hazelnut	0.83	0.97	0.96	0.99
metal nut	0.88	0.98	0.97	0.81
pill	0.84	0.93	0.90	0.93
screw	0.84	0.86	0.96	0.94
toothbrush	1.00	0.98	1.00	1.00
transistor	0.91	0.95	0.96	0.99
zipper	0.98	0.99	0.99	0.98
avg. objects	0.90	0.94	0.93	0.93
avg. all	0.91	0.95	0.95	0.95

TABLE 4

Experimental comparison of two proposed training objectives given as **AUROC** on the pixel-level and image-level for each texture category in the MVTec AD dataset.

Category	pixel-level		image-level	
	Obj. (1)	Obj. (2)	Obj. (1)	Obj. (2)
carpet	1.00	0.99	0.98	1.00
grid	1.00	0.99	1.00	0.96
leather	0.99	0.97	1.00	0.95
tile	0.99	0.97	1.00	0.99
wood	0.98	0.99	0.99	0.97
avg. all	0.99	0.98	0.99	0.97

anomalous regions in images. For practical cases we can use either of the two to get an accurate model. In the following, we discuss some important differences of the two approaches.

The objective (1) is a more robust and practical choice to work with. There is a good measure of training progress given by the reconstruction error, which strongly correlates with the ability of the model to remove anomalous patterns from images. Therefore, reconstruction error provides a good choice for our target loss. Also the search for the weighting parameter λ is rather straightforward – setting $\lambda = 0.5$ turns out to be sufficiently good. Furthermore, elastic deformation as a distortion technique seems to provide enough discriminative information during training to detect various kinds of anomalous patterns in the application phase. Interestingly, a corresponding model tends to act as a filter for anomalous patterns by replacing irregularities with locally consistent reconstructions. Therefore, it can also detect difficult anomalous examples, which lie very close to the data manifold of normal examples.

The objective (2) produces a model, which behaves more similar to a segmentation network. Therefore, it can potentially provide more accurate segmentation results. For the same reason, the objective (2) is more sensitive to the choice of modification method that we use during training to create corrupted examples. Therefore, it is more prone

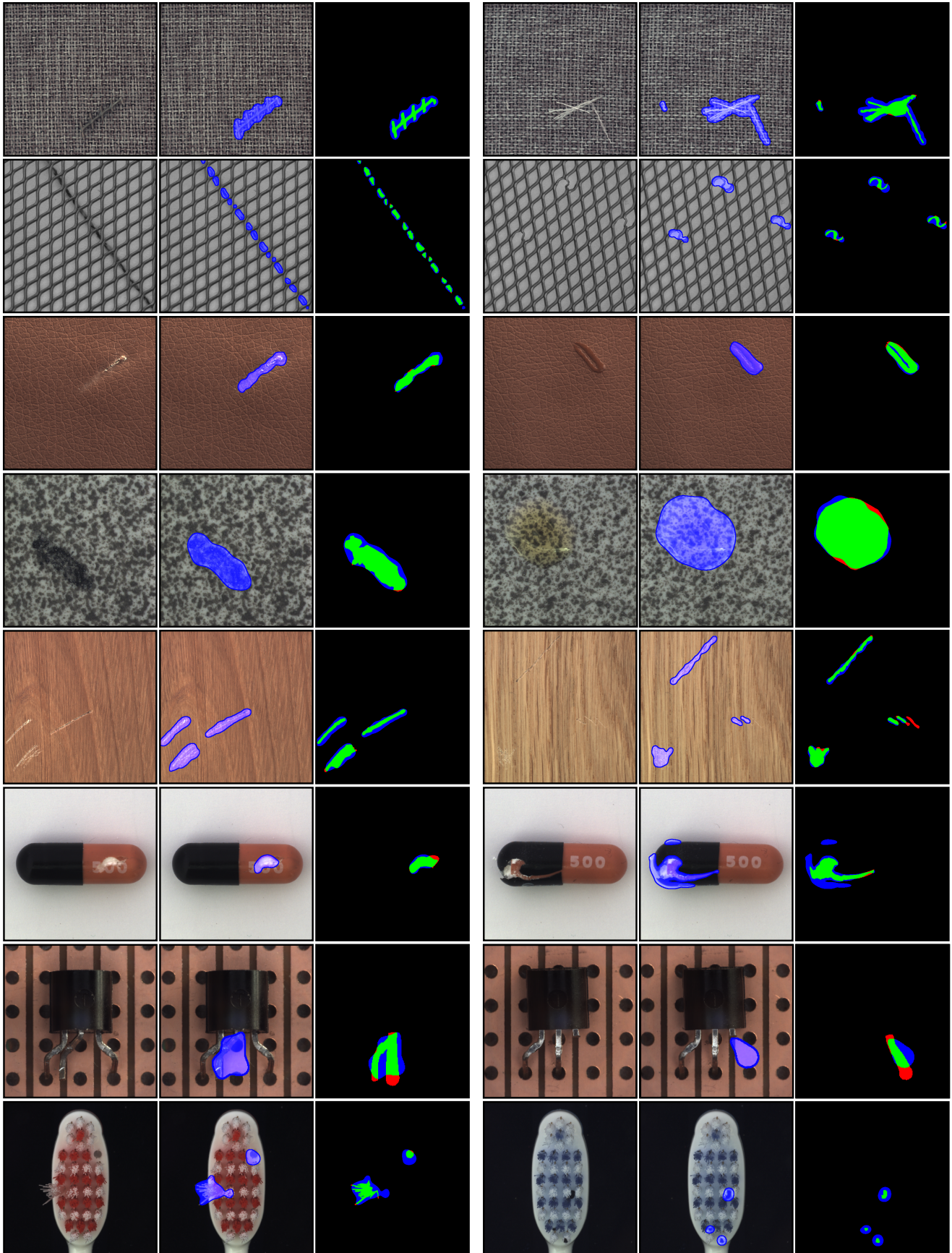


Fig. 7. Illustration of anomaly segmentation results when training according to the objective (1). Each row shows two random examples from the texture and some object categories in the MVTeC data set. The columns show the input image, the prediction mask for the anomalous regions and the evaluation map with respect to the ground truth masks provided with the data set. The colors green, blue and red in the evaluation map encode the true positives, false positives and false negatives, respectively.

to overfitting and we must rely on early stopping to get accurate results. Also the search for good λ values is more difficult because the second term in the objective (2) tends to influence the training in a less predictable way. Despite these difficulties the increase in the localization performance can be very significant in comparison to objective (1) as we showed in Figure 6 for the case of glue drops on a wooden surface. We plan on investigating how the specific form of image modifications affects the overfitting during training in the future works. It is worth mentioning that training a model in a supervised way by using a segmentation loss directly on the artificially generated anomalies does not provide good results. It begins to overfit on the specific type of chosen artificial patterns already after a few training epochs. For example, it quickly learns to locate the elastic deformation patterns but completely fails to recognize real anomalies from the test set.

As a final remark we note that the results in Table 4 suggest a potential improvement by combining both models trained separately via objective (1) and (2) in an ensemble.

5 CONCLUSION

We presented a self-supervised learning framework for the task of visual anomaly detection by training a deep convolutional autoencoder on partially distorted images with one of two proposed objectives. Our approach benefits from using discriminative information during training which allows it to better distinguish between normal and anomalous regions in the testing phase. A model trained via objective (1) acts, in some sense, as a filter for anomalous patterns by replacing irregularities with locally consistent reconstructions. Due to this fact, it is capable of detecting a variety of anomalous patterns - even those which lie very close to the data manifold populated by the normal examples. When training with objective (2) the resulting model, on the one hand, aims to reconstruct the normal regions resulting in a low reconstruction error and on the other hand it amplifies the reconstruction error for the anomalous regions acting almost as a segmentation network. This potentially allows to boost final localization performance - as we showed in the experimental section in Figure 5. In contrast to the pure segmentation approach, however, the resulting model focuses on the data manifold reducing overfitting on specific patterns produced by a chosen transformation to create distorted inputs. Finally, the inference with our method (during training and prediction) is very efficient. Unlike related previous methods, it processes the entire input image in one single step. In our experiments on the publicly available MVTec Anomaly Detection dataset we showed that the new approach achieves (on average) a higher recognition and localization performance. On the texture-subset, in particular, it consistently outperforms a bunch of recent anomaly detection methods by a big margin.

REFERENCES

- [1] B. Schölkopf, J. C. Platt, J. Shawe-Taylor, A. J. Smola, and R. C. Williamson, "Estimating the support of a high-dimensional distribution," *Neural Comput.*, vol. 13, no. 7, pp. 1443–1471, 2001.
- [2] L. Ruff, N. Görnitz, L. Deecke, S. A. Siddiqui, R. A. Vandermeulen, A. Binder, E. Müller, and M. Kloft, "Deep one-class classification," in *Proceedings of the 35th International Conference on Machine Learning, ICML 2018, Stockholm, Sweden, July 10-15, 2018*, ser. Proceedings of Machine Learning Research, J. G. Dy and A. Krause, Eds., vol. 80. PMLR, 2018, pp. 4390–4399.
- [3] M. Haselmann, D. P. Gruber, and P. Tabatabai, "Anomaly detection using deep learning based image completion," in *17th IEEE International Conference on Machine Learning and Applications, ICMLA 2018, Orlando, FL, USA, December 17-20, 2018*, M. A. Wani, M. M. Kantardzic, M. S. Mouchaweh, J. Gama, and E. Lughofer, Eds. IEEE, 2018, pp. 1237–1242.
- [4] P. Bergmann, S. Löwe, M. Fauser, D. Sattlegger, and C. Steger, "Improving unsupervised defect segmentation by applying structural similarity to autoencoders," in *Proceedings of the 14th International Joint Conference on Computer Vision, Imaging and Computer Graphics Theory and Applications, VISIGRAPP 2019, Volume 5: VISAPP, Prague, Czech Republic, February 25-27, 2019*, A. Trémeau, G. M. Farinella, and J. Braz, Eds. SciTePress, 2019, pp. 372–380.
- [5] L. Wang, D. Zhang, J. Guo, and Y. Han, "Image anomaly detection using normal data only by latent space resampling," *Applied Sciences*, vol. 10, no. 23, 2020.
- [6] P. Bergmann, M. Fauser, D. Sattlegger, and C. Steger, "Uninformed students: Student-teacher anomaly detection with discriminative latent embeddings," in *2020 IEEE/CVF Conference on Computer Vision and Pattern Recognition, CVPR 2020, Seattle, WA, USA, June 13-19, 2020*. Computer Vision Foundation / IEEE, 2020, pp. 4182–4191.
- [7] S. Venkataraman, K. Peng, R. V. Singh, and A. Mahalanobis, "Attention guided anomaly localization in images," in *Computer Vision - ECCV 2020 - 16th European Conference, Glasgow, UK, August 23-28, 2020, Proceedings, Part XVII*, ser. Lecture Notes in Computer Science, A. Vedaldi, H. Bischof, T. Brox, and J. Frahm, Eds., vol. 12362. Springer, 2020, pp. 485–503.
- [8] T. Schlegl, P. Seeböck, S. M. Waldstein, U. Schmidt-Erfurth, and G. Langs, "Unsupervised anomaly detection with generative adversarial networks to guide marker discovery," in *Information Processing in Medical Imaging - 25th International Conference, IPMI 2017, Boone, NC, USA, June 25-30, 2017, Proceedings*, ser. Lecture Notes in Computer Science, M. Niethammer, M. Styner, S. R. Aylward, H. Zhu, I. Oguz, P. Yap, and D. Shen, Eds., vol. 10265. Springer, 2017, pp. 146–157.
- [9] P. Napolitano, F. Piccoli, and R. Schettini, "Anomaly detection in nanofibrous materials by cnn-based self-similarity," *Sensors*, vol. 18, no. 1, p. 209, 2018.
- [10] T. Böttger and M. Ulrich, "Real-time texture error detection on textured surfaces with compressed sensing," *Pattern Recognit. Image Anal.*, vol. 26, pp. 88–94, 2016.
- [11] W. Liu, R. Li, M. Zheng, S. Karanam, Z. Wu, B. Bhanu, R. J. Radke, and O. I. Camps, "Towards visually explaining variational autoencoders," in *2020 IEEE/CVF Conference on Computer Vision and Pattern Recognition, CVPR 2020, Seattle, WA, USA, June 13-19, 2020*. IEEE, 2020, pp. 8639–8648.
- [12] D. M. J. Tax and R. P. W. Duin, "Support vector data description," *Mach. Learn.*, vol. 54, no. 1, pp. 45–66, 2004.
- [13] P. Chong, L. Ruff, M. Kloft, and A. Binder, "Simple and effective prevention of mode collapse in deep one-class classification," in *2020 International Joint Conference on Neural Networks, IJCNN 2020, Glasgow, United Kingdom, July 19-24, 2020*. IEEE, 2020, pp. 1–9.
- [14] C. Hu, Y. Feng, H. Kamigaito, H. Takamura, and M. Okumura, "One-class text classification with multi-modal deep support vector data description," in *Proceedings of the 16th Conference of the European Chapter of the Association for Computational Linguistics: Main Volume, EACL 2021, Online, April 19 - 23, 2021*, P. Merlo, J. Tiedemann, and R. Tsarfaty, Eds. Association for Computational Linguistics, 2021, pp. 3378–3390.
- [15] C. Li, K. Sohn, J. Yoon, and T. Pfister, "Cutpaste: Self-supervised learning for anomaly detection and localization," in *IEEE Conference on Computer Vision and Pattern Recognition, CVPR 2021, virtual, June 19-25, 2021*. Computer Vision Foundation / IEEE, 2021, pp. 9664–9674.
- [16] J. Pirnay and K. Chai, "Inpainting transformer for anomaly detection," in *Image Analysis and Processing - ICIAP 2022 - 21st International Conference, Lecce, Italy, May 23-27, 2022, Proceedings, Part II*, ser. Lecture Notes in Computer Science, S. Sclaroff, C. Distanto, M. Leo, G. M. Farinella, and F. Tombari, Eds., vol. 13232. Springer, 2022, pp. 394–406.

- [17] P. Vincent, H. Larochelle, Y. Bengio, and P. Manzagol, "Extracting and composing robust features with denoising autoencoders," in *Machine Learning, Proceedings of the Twenty-Fifth International Conference (ICML 2008), Helsinki, Finland, June 5-9, 2008*, ser. ACM International Conference Proceeding Series, W. W. Cohen, A. McCallum, and S. T. Roweis, Eds., vol. 307. ACM, 2008, pp. 1096–1103.
- [18] J. Deng, Z. Zhang, E. Marchi, and B. W. Schuller, "Sparse autoencoder-based feature transfer learning for speech emotion recognition," in *2013 Humaine Association Conference on Affective Computing and Intelligent Interaction, ACII 2013, Geneva, Switzerland, September 2-5, 2013*. IEEE Computer Society, 2013, pp. 511–516.
- [19] D. Pathak, P. Krähenbühl, J. Donahue, T. Darrell, and A. A. Efros, "Context encoders: Feature learning by inpainting," in *2016 IEEE Conference on Computer Vision and Pattern Recognition, CVPR 2016, Las Vegas, NV, USA, June 27-30, 2016*. IEEE Computer Society, 2016, pp. 2536–2544.
- [20] S. Iizuka, E. Simo-Serra, and H. Ishikawa, "Globally and locally consistent image completion," *ACM Trans. Graph.*, vol. 36, no. 4, pp. 107:1–107:14, 2017.
- [21] J. Yu, Z. Lin, J. Yang, X. Shen, X. Lu, and T. S. Huang, "Generative image inpainting with contextual attention," in *2018 IEEE Conference on Computer Vision and Pattern Recognition, CVPR 2018, Salt Lake City, UT, USA, June 18-22, 2018*. IEEE Computer Society, 2018, pp. 5505–5514.
- [22] G. Liu, F. A. Reda, K. J. Shih, T. Wang, A. Tao, and B. Catanzaro, "Image inpainting for irregular holes using partial convolutions," in *Computer Vision - ECCV 2018 - 15th European Conference, Munich, Germany, September 8-14, 2018, Proceedings, Part XI*, ser. Lecture Notes in Computer Science, V. Ferrari, M. Hebert, C. Sminchisescu, and Y. Weiss, Eds., vol. 11215. Springer, 2018, pp. 89–105.
- [23] J. Yu, Z. Lin, J. Yang, X. Shen, X. Lu, and T. S. Huang, "Free-form image inpainting with gated convolution," in *2019 IEEE/CVF International Conference on Computer Vision, ICCV 2019, Seoul, Korea (South), October 27 - November 2, 2019*. IEEE, 2019, pp. 4470–4479.
- [24] P. Bergmann, M. Fauser, D. Sattlegger, and C. Steger, "Mvtec AD - A comprehensive real-world dataset for unsupervised anomaly detection," in *IEEE Conference on Computer Vision and Pattern Recognition, CVPR 2019, Long Beach, CA, USA, June 16-20, 2019*. Computer Vision Foundation / IEEE, 2019, pp. 9592–9600.
- [25] P. Bergmann, K. Batzner, M. Fauser, D. Sattlegger, and C. Steger, "The mvtec anomaly detection dataset: A comprehensive real-world dataset for unsupervised anomaly detection," *Int. J. Comput. Vis.*, vol. 129, no. 4, pp. 1038–1059, 2021.
- [26] V. Zavrtanik, M. Kristan, and D. Skocaj, "Reconstruction by inpainting for visual anomaly detection," *Pattern Recognit.*, vol. 112, p. 107706, 2021.
- [27] R. R. Selvaraju, M. Cogswell, A. Das, R. Vedantam, D. Parikh, and D. Batra, "Grad-cam: Visual explanations from deep networks via gradient-based localization," *Int. J. Comput. Vis.*, vol. 128, no. 2, pp. 336–359, 2020.
- [28] D. P. Kingma and J. Ba, "Adam: A method for stochastic optimization," in *3rd International Conference on Learning Representations, ICLR 2015, San Diego, CA, USA, May 7-9, 2015, Conference Track Proceedings*, Y. Bengio and Y. LeCun, Eds., 2015.
- [29] P. Liznerski, L. Ruff, R. A. Vandermeulen, B. J. Franks, M. Kloft, and K. Müller, "Explainable deep one-class classification," in *9th International Conference on Learning Representations, ICLR 2021, Virtual Event, Austria, May 3-7, 2021*. OpenReview.net, 2021.